Structural studies of Nd-modified lead zirconate titanate ceramics between 11 and 680 K at the morphotropic phase boundary

J. Frantti and V. Lantto
Microelectronics and Material Physics Laboratories, University of Oulu, P.O. Box 400, 90571 Oulu, Finland
(Received 13 November 1996; revised manuscript received 27 January 1997)

Raman spectroscopy between 11 and 680 K was used together with room-temperature x-ray-diffraction experiments for structural studies of ferroelectric Nd-modified lead zirconate titanate ceramics at the morphotropic phase boundary. The Nd addition was found to have a strong effect on the balance between tetragonal and trigonal phases in the structure. The tetragonal phase fraction increased and the size of trigonal domains decreased with the increasing Nd addition. The tetragonal c/a ratio was found to increase at small Nd concentrations below 1% of the A-cation sites and then decrease again at higher concentrations. A similar behavior was found also with the Nd addition into $PbTiO_3$ ceramics, but the c/a ratio had a maximum at Nd concentrations of around 0.1%. Raman results revealed a subpeak structure of tetragonal $A_1(1TO)$-mode frequencies in agreement with earlier findings in $PbTiO_3$ single crystals and ceramics. The observed subpeak frequencies of the $A_1(1TO)$ mode were approximately fit by energy levels of an anharmonic double-well potential both in symmetric (paraelectric) and asymmetric (ferroelectric) forms from the mean-field approach. In addition to the four subpeaks, an additional mode was also found at about 55 cm^{-1}. Peak fit together with the second derivatives of Raman spectra were used to reveal different Raman peaks from tetragonal and trigonal phases in the intermediate-frequency region between 180 and 400 cm^{-1}. The high-temperature Raman spectra from the samples were compared with spectra measured from $Pb_{0.865}La_{0.09}(Zr_{0.65}Ti_{0.35})O_3$ ceramics which is a well-known relaxor material. [S0163-1829(97)01325-8]

I. INTRODUCTION

The composition of technologically important $Pb(Zr_xTi_{1-x})O_3$ ceramics, PZT's, is around the morphotropic phase boundary (MPB) ($x=0.53$ at room temperature[1]) where the tetragonal and trigonal phases in the phase diagram have equal Gibbs free energies. In polycrystalline ceramics there is a coexistence region between the tetragonal and trigonal phases at compositions around the MPB, which has very important effects on the properties of these ceramics. Trivalent lanthanide additives like La and Nd influence the balance between the two phase fractions and also decrease significantly the Curie temperature T_C. These additives also have a strong effect on the size of the ferroelectric domains in PZT's. For instance, in Ref. 2 it was found possible to induce a relaxorlike behavior at around room temperature in the whole tetragonal phase region $0 \leqslant x \leqslant 0.53$ with increasing La content in La-modified PZT's (PLZT's). La concentrations for the normal ferroelectric to relaxor transformation at about room temperature, from the tetragonal PLZT phase diagram in Ref. 2, are about 23 and 10% of the A-cation sites in $PbTiO_3$ (PT) and PZT at the MPB, respectively. The transformation between normal and relaxorlike behaviors was found to be associated with domain evolution from normal micron-sized domains to tweedlike subdomain structures and finally to polar nanodomains,[2] which are now under intensive study.[3–5] In the case of very small domains, structure determination, e.g., from x-ray-diffraction and Raman results may seem confusing, since x-ray diffraction probes long-range order whereas Raman is, in principle, a ''local'' probe.

In our earlier study[6] low-temperature Raman spectroscopy between 11 K and room temperature was used together with room-temperature x-ray-diffraction experiments to study the effects of Nd addition in ferroelectric $PbTiO_3$ ceramics. Here we report similar studies at the other end of the tetragonal region of PZT's (at MPB; $x=0.53$). We have now used Raman spectroscopy from an ambient temperature of 11 K up to a temperature above the Curie temperature T_C together with room-temperature x-ray-diffraction experiments to study the structural effects of Nd addition into $Pb_{1-3y/2}Nd_y(Zr_{0.53}Ti_{0.47})O_3$ ceramics in the Nd-concentration region y between 0 and 4%. Now we study the structural effects of Nd addition also at low Nd concentrations $y=0.25$, 0.50, and 0.75% and also make some comparative studies at low Nd concentrations $y=0.12$, 0.25, and 0.5 % in $PbTiO_3$. The well-known relaxor material 9/65/35 PLZT [$Pb_{0.865}La_{0.09}(Zr_{0.65}Ti_{0.35})O_3$] was also used as a reference material for Raman studies.

The transition elements Ti and Zr occupy the octahedral cages of the B-site cations in the perovskite structure of PZT's. There is competition between the tetragonal and trigonal phases at compositions around the MPB. In the case of $PbTiO_3$, the results in Ref. 7 show that hybridization of Ti3d states with O2p states is the origin of ferroelectricity in the structure and strong hybridization occurs also between Pb6s and O2p states, which leads to the large strain that stabilizes the tetragonal phase. Zr^{4+} ions with the ionic radius of 0.87 Å are larger than the Ti^{4+} ions (radius 0.64 Å) and make the lattice constant a and the cuboctahedral cages for the Pb^{2+} ions in the A sites larger. With increasing a the

tetragonal c/a ratio decreases at room temperature from 1.064 in $PbTiO_3$ (Ref. 6) down to 1.023 in PZT at the MPB (Fig. 2), which means also a decrease in T_C by more than 100 K.[1] Inside their oxygen octahedra the larger Zr^{4+} ions may also tend to be displaced in the [111] direction and favor the trigonal phase. The [001] displacement of the Ti^{4+} ions in the tetragonal phase contracts the a axis,[8] while the larger Zr^{4+} ions tend to hinder this behavior. In the trigonal phase at the high-Zr side, the low tetragonal strain is no longer able to prevent the Zr octahedra to force also the Ti octahedra trigonal. A discussion of the possible defect structure and charge compensation originating in the Nd addition into PNT ceramics was given in Ref. 6.

The cubic phase of PZT's in the paraelectric state above T_C has the space group O_h^1 and exhibits no first-order Raman effect. The trigonal phases (space groups C_{3v}^1 and C_{3v}^6) and the tetragonal phase (C_{4v}^1) have Raman-active modes and the irreducible representations of these modes are given, e.g., in Ref. 9. We use here the labeling scheme introduced by Burns and Scott[10] for the optical A_1, B_1, and E modes in the tetragonal phase. Our results in Ref. 6 revealed a subpeak structure of the tetragonal $A_1(1\mathrm{TO})$-mode frequencies in pure and Nd-modified $PbTiO_3$ ceramics in agreement with earlier findings in $PbTiO_3$ single crystals.[11] It was also possible to find, on the basis of *ab initio* computational results in Ref. 7, an anharmonic double-well potential with $A_1(1\mathrm{TO})$-mode vibrations which fit approximately the observed subpeak frequencies in $PbTiO_3$.[6] A similar subpeak structure was also revealed here by a peak fit of the measured Raman spectra of pure and Nd-modified PZT samples at the MPB. In addition to a symmetric and anharmonic double-well potential (similar to that in Ref. 6), an asymmetric double-well potential from the mean-field approach[12] was also used in order to fit the observed subpeak frequencies of the $A_1(1\mathrm{TO})$-mode vibrations.

II. EXPERIMENT

Ceramic PNZT samples prepared from high-purity oxides by Siemens in Germany[6] were in the form of discs with a diameter of 13 mm and thickness of 1 mm. The Nd content y in the samples was between 0 and 4% of the A cation sites. The PNT samples were prepared in our laboratory from commercial lead-titanate ($>99\%$) and Nd_2O_3 powders through a usual ceramic route (sintering at 1150 °C) and had different Nd concentrations $y=0$, 0.12, 0.25, and 0.50% in the nominal composition $Pb_{1-3y/2}Nd_yTiO_3$. X-ray diffraction with Cu$K\alpha$ radiation was used to study the room-temperature structure of the samples. The behavior of the lattice constants with Nd concentration y in the structure of both PNZT and PNT samples was carefully studied by using a polycrystalline silicon as a calibration standard. Milling of the PNT samples with $y=0$ and 0.12% was necessary before the x-ray-diffraction measurements in order to decrease the grain size of the ceramics after sintering. The PNT samples with $y=0.25$ and 0.50% were in the form of pressed discs, but the discs from the powders with $y=0$ and 0.12% broke down into powder form during sintering.

Raman spectra were measured using the Jobin-Yvon T-64000 spectrometer with a charge-coupled-device detector. The 514.532 nm line of an Ar^+ laser was used in the measurements which were made at two different setups with a mercury lamp (strong line at 1122.60 cm^{-1}) as a calibration standard for the Raman peaks. The micro-Raman utility was used to measure some of the room-temperature spectra from the discs at a backscattering configuration. Spectra from various PNZT discs at various ambient temperatures between 11 and 295 K were measured in a macrochamber using the same experimental setup as in Ref. 6. Power of the laser beam on samples was between 5 and 8 mW with a spot diameter of some tens of micrometers. In the high-temperature measurements the samples were installed inside an oven and a thermocouple, fixed at the surface of the sample, was used to measure the temperature.

III. X-RAY-DIFFRACTION EXPERIMENTS

Cu$K\alpha$ doublet (1.540 56 and 1.544 39 Å) was used for recording the x-ray-diffraction patterns from the samples at room temperature. A procedure similar to that in Ref. 6 was used to determine the lattice constants of different $Pb_{1-3y/2}Nd_y(Zr_{0.53}Ti_{0.47})O_3$ samples. The coexistence of the trigonal and tetragonal phases caused some inaccuracy in the results at low Nd concentrations y, because of the overlapping of the characteristic x-ray-diffraction peaks, and the tetragonal lattice constants were most accurate for samples with $y=3.0$ and 4.0%. The tetragonal c/a ratio was taken from the d_{002}/d_{200} ratio. The diffraction angles for tetragonal (200), (002), and trigonal {200} reflections were determined by a commercial curve-fit program from the x-ray-diffraction patterns measured at a discrete set of angles (typically at intervals of 0.07°) over the characteristic 2θ region. In fact, the time corresponding to an arrival of 40 000 pulses to the detector was measured at each 2θ angle which made possible an accurate determination of the intensity (in cps). Figure 1 shows the x-ray-diffraction patterns measured at room temperature from PNZT samples with y between 0 and 4.0%.

Figure 2 shows the tetragonal lattice constants a and c together with the c/a ratio and the cube root of the unit-cell volume $(a^2c)^{1/3}$ as a function of the Nd concentration y from the peak-fit results in Fig. 1. The initial decrease in the c/a ratio in Fig. 2 may originate in small inaccuracies in the values of a for the samples with $y=0$ and 0.25% because of the strong overlap of the trigonal and tetragonal (200)-reflection peaks in the corresponding patterns in Fig. 1. Because of a poling treatment before the x-ray-diffraction measurements, the fitted peak intensities in Fig. 1 [e.g., the intensity ratio between the tetragonal (200) and (002) peaks] do not correspond to a random grain (domain) orientation in the samples. After an initial increase, the lattice constant c, in Fig. 2, turns to decrease with the increasing Nd concentration y above about 1.0%. Correspondingly, the c/a ratio has a maximum at around $y=0.75\%$.

It was found in Ref. 6 that the c/a ratio in $Pb_{1-3y/2}Nd_yTiO_3$ ceramics decreased with increasing Nd concentration y above 2.0%. In order to test if there is a possible maximum in the c/a ratio also in PNT ceramics at low Nd concentrations, we made a careful study of the lattice constants in pure and Nd-modified ($y=0.12\%$) lead titanate ceramics. The lattice constants were determined from (403), (242), (332), and (142) reflections for a pure lead titanate powder and from (115), (242), (332), and (142) reflections

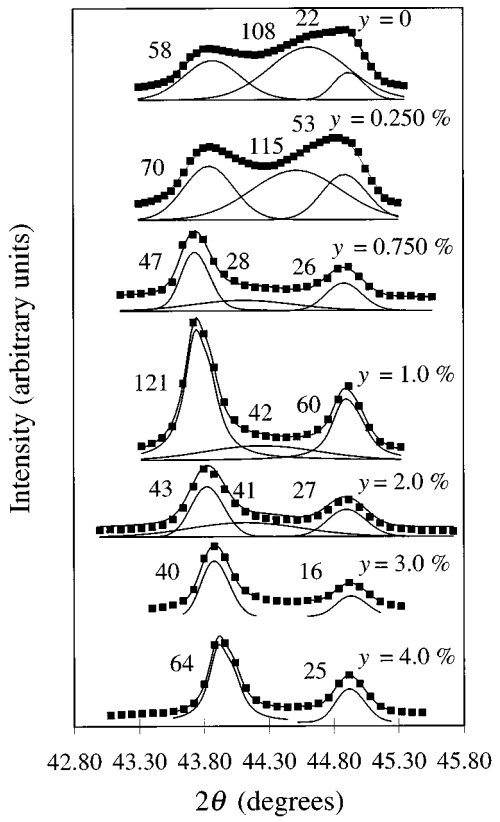

FIG. 1. X-ray-diffraction patterns of tetragonal (002), (200), and trigonal {200} reflections measured from $Pb_{1-3y/2}Nd_y(Zr_{0.53}Ti_{0.47})O_3$ samples with $y=0$, 0.25, 0.75, 1.0, 2.0, 3.0, and 4.0 % together with the results of a peak fit for each pattern. The figures refer to relative peak intensities from the fit.

for Nd-modified powders using a procedure similar to that in Ref. 6. The peak angles were determined with the same procedure as was used above for the PNZT samples. The same value 3.9002 Å was obtained for the lattice constant a in both ceramics, while the lattice constant c had values 4.1516 and 4.1524 Å in pure and Nd-modified ($y=0.12\%$) ceramics, respectively. Therefore, the c/a ratio increased from 1.0645 in pure ceramics up to 1.0647 at the Nd concentration of $y=0.12\%$. At higher Nd concentrations ($y=0.25$ and 0.50 %) the c/a ratio decreased with increasing Nd concentration in agreement with the results in Ref. 6. The sensitivity of the lattice constants of lead titanate ceramics to small impurity contents may be an explanation for the variance in the reported values of the lattice constants given in the literature for tetragonal lead titanate.

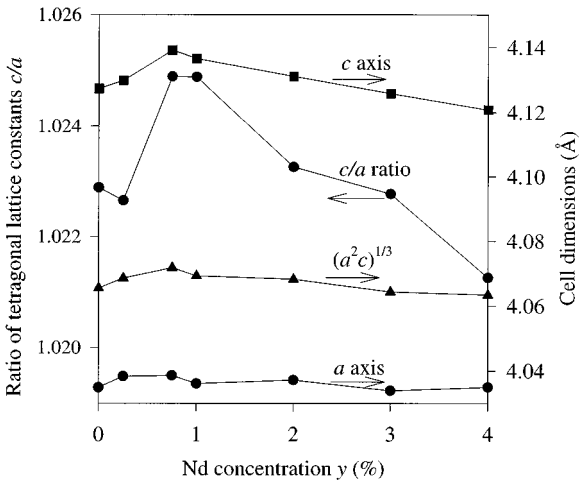

FIG. 2. Tetragonal lattice constants a and c, the ratio c/a, and the cubic root of the unit-cell volume as a function of Nd concentration in $Pb_{1-3y/2}Nd_y(Zr_{0.53}Ti_{0.47})O_3$ ceramics.

The x-ray-diffraction patterns in Fig. 1 show that strong structural changes follow from the addition of Nd into the PZT ceramics at the morphotropic phase boundary. A large amount of the trigonal phase in the pure PZT ($y=0$) seems to disappear already at the Nd concentration $y=0.75\%$. The peak fit, however, reveals the situation more exactly. A reason for the ''disappearance'' of the trigonal {200}-peak intensity is broadening of the peak with the increasing Nd content. This means that the average size of trigonal domains decreases with the increasing Nd content. It was possible to calculate from the HWHM values $\Delta(2\theta)$ of the trigonal {200} peaks in Fig. 1 the average size L of the trigonal domains using the Scherrer equation $\Delta(2\theta)=0.89\lambda/(L\cos\theta)$ where λ is the wavelength of x rays. The results for L after a correction for the Cu $K\alpha$ doublet (Rachinger correction) were 285, 252, 218, and 195 Å in PNZT samples in Fig. 1 with $y=0$, 0.25, 0.75, and 1.0 %, respectively.

The fitted results in Fig. 1 show that the spacing between the trigonal (200) planes increases with increasing Nd concentration. Similarly, they clearly show an initial increase in the tetragonal lattice constant c with Nd addition and a maximum at $y=0.75\%$, as plotted in Fig. 2. The c/a ratio in Fig. 2 has a similar behavior, since the value of the lattice constant a is less sensitive to Nd addition. A similar initial increase and a maximum in the c/a ratio was also found in Ref. 13 when Sb^{5+} ions were introduced into the B-cation sites in PZT ceramics. The maximum c/a ratio appeared at an Sb concentration of 0.5% of the B-cation sites.[13] $PbTiO_3$ and PZT ceramics without additives exhibit p-type extrinsic conductivity, and usually, lanthanum at concentrations of about 0.1 and 0.5 % of the A-cation sites is used to remove the conductivity of $PbTiO_3$ and PZT ceramics, respectively.[1] The origin of the p-type conductivity in PT and PZT ceramics may relate to Pb^{4+} ions in the B-cation sites which also evaporate as divalent ions in PbO during sintering and leave holes into the valence band. The ionic radii 0.64, 0.87, and 0.84 Å of Ti^{4+}, Zr^{4+}, and Pb^{4+} ions, respectively, explain the higher hole concentrations in PZT ceramics.

An explanation for the initial increase of the lattice constant c and the c/a ratio in Fig. 2 may be in the electronic charge compensation at low Nd^{3+} concentrations in the A-cation sites (or at low Sb^{5+} concentrations in the B-cation sites in Ref. 13). It was found in Ref. 14 from band-structure calculations and electron-paramagnetic-resonance (EPR) results that Pb6s lone-pair orbitals comprise a part of the valence-band maximum both in PT and PZT structures which leads to shallow A-site hole traps and to Pb^{3+} ions in conductive ceramics. The large Pb displacements which lead to the large tetragonal strain (c/a ratio) and stabilize the tetragonal phase can be attributed, in part, to the large repulsion between the polarized lone-pair-electron

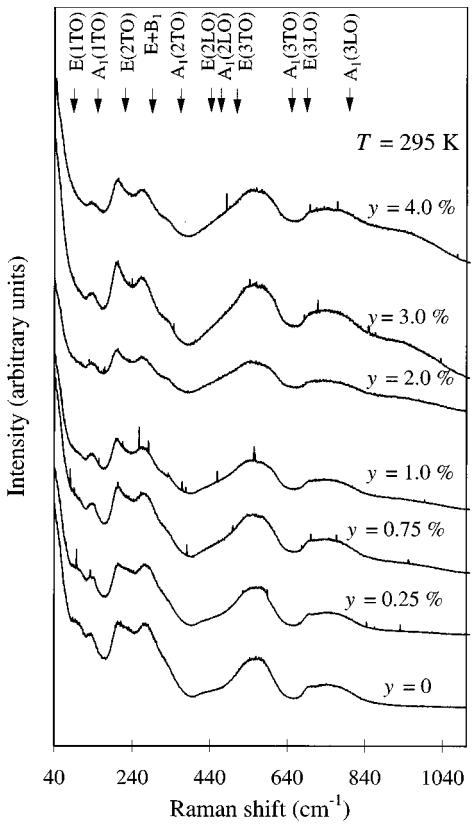

FIG. 3. Raman spectra measured at room temperature from different $Pb_{1-3y/2}Nd_y(Zr_{0.53}Ti_{0.47})O_3$ samples with y between 0 and 4.0 %. Positions of different Raman peaks at room temperature in $PbTiO_3$ (Ref. 7) are also shown at the top. There are a few very sharp spikes in the spectra which do not correspond to any real Raman peaks, but probably originate in cosmic rays in the CCD detector.

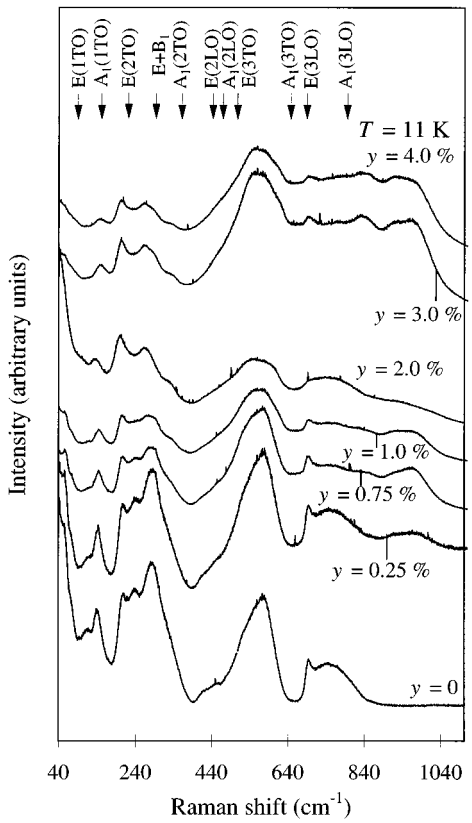

FIG. 4. Raman spectra measured at an ambient cryostat temperature of 11 K from different $Pb_{1-3y/2}Nd_y(Zr_{0.53}Ti_{0.47})O_3$ samples with y between 0 and 4.0 %. The positions of different Raman peaks at room temperature in $PbTiO_3$ (Ref. 7) are also shown at the top.

charge of the Pb^{2+} ions and the oxygen plane in a similar way as in α-PbO structure (compare Fig. 1 in Ref. 6). However, the repulsion is missing from the hole-trapped Pb^{3+} ions, to a large extent. Therefore, an electronic compensation with Nd^{3+} ions in the A-cation sites removes the ineffective Pb^{3+} ions and may increase the tetragonality in the structure. With increasing Nd addition the electronic compensation changes to vacancy compensation with vacancies in the A-cation sites and then the c/a ratio begins to decrease, as seen in Fig. 2. In $PbTiO_3$ ceramics with a lower hole concentration, the c/a ratio has a maximum at lower Nd additions. Therefore, the increase in the c/a ratio in our PNZT ceramics was about three times higher than in the tested PNT ceramics.

IV. RAMAN EXPERIMENTS

Figures 3 and 4 show the Raman spectra measured from $Pb_{1-3y/2}Nd_y(Zr_{0.53}Ti_{0.47})O_3$ samples with various y values between 0 and 4.0% at room temperature and at an ambient cryostat temperature of 11 K, respectively. Similar spectra were also measured at ambient temperatures of 100, 150, and 200 K. The high-temperature Raman spectra measured from our PNZT samples with $y=0$ and 3.0 % are shown in Figs. 5 and 6, respectively. The Curie temperature, T_C, of pure PZT ceramics at the MPB ($x=0.53$) is about 650 K (Ref. 1) and, thus, the highest temperatures 671 and 676 K in Figs. 5 and 6, respectively, are in the paraelectric temperature region where the first-order Raman peaks should not exist. Raman spectra were also measured from 9/65/35 PLZT relaxor ceramics at ambient cryostat temperatures of 11, 100, 150, 200, and 295 K and the spectra are shown in Fig. 7. All the five spectra in Fig. 7 have about the same shape which is also very similar to the shape of the high-temperature spectra at 671 and 676 K in Figs. 5 and 6, respectively. In addition to the Stokes spectra in Figs. 3, 4, and 7, the corresponding anti-Stokes spectra were also measured at ambient temperatures of 11, 100, 150, 200, and 295 K. In order to find the positions, line widths and intensities of different Raman peaks in the measured spectra, a peak fit was made for the most of the Stokes and anti-Stokes spectra.

The temperature values here refer to ambient temperatures inside the cryostat. However, the excitation of phonons by laser light causes a local heating[6,16] in which case the temperatures are calculated from the intensity ratio between corresponding anti-Stokes and Stokes lines according to the equation

$$I(\text{anti-Stokes})/I(\text{Stokes})=\exp(-\hbar\omega/k_BT) \qquad (1)$$

for a first-order Raman line. $\hbar\omega$ is the quantum energy of the phonon. The local heating calculated from Eq. (1) was found to be remarkable, especially at low temperatures, which re-

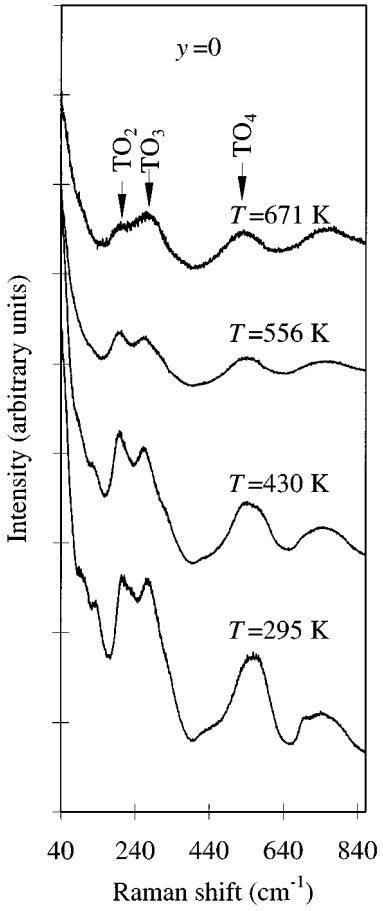

FIG. 5. Raman spectra measured at different temperatures between 295 K and 671 K from a $Pb(Zr_{0.53}Ti_{0.47})O_3$ sample. The positions of the TO_2, TO_3, and TO_4 peaks in the relaxor state above T_C are also shown.

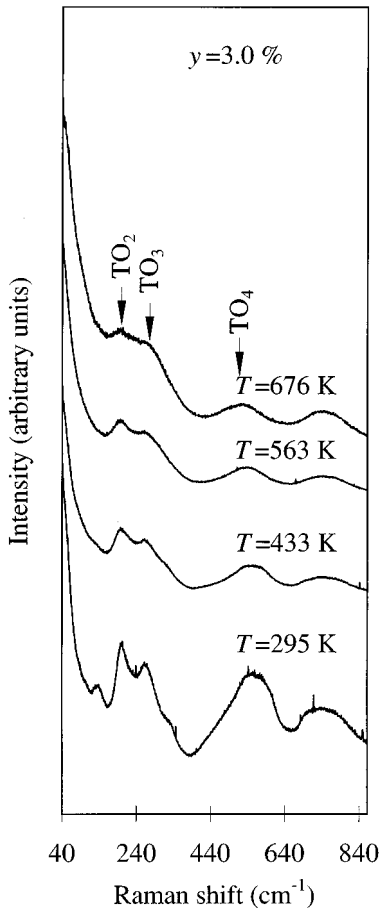

FIG. 6. Raman spectra measured at different temperatures between 295 and 676 K from a $Pb_{0.955}Nd_{0.03}(Zr_{0.53}Ti_{0.47})O_3$ sample. The positions of the TO_2, TO_3, and TO_4 peaks in the relaxor state above T_C are also shown.

flects a strong decrease in the heat capacity according to the Debye T^3 law at low temperatures.

A. The low-frequency region below 180 cm^{-1}

In the analysis of low-temperature Raman spectra (Figs. 3 and 4) we concentrate on the low-frequency region below 180 cm^{-1} and on the intermediate-frequency region between 180 and 400 cm^{-1}. In the low-frequency region the Raman spectra in Figs. 3 and 4 reveal a similar subpeak structure which was also found in the Nd-modified lead titanate ceramics in Ref. 6. The origin of the subpeaks has been related to an anharmonic double-well potential for the $A_1(1TO)$-mode vibrations.[6,11] A well-known additional mode in PZT ceramics between 50 and 60 cm^{-1} is also clearly seen in Figs. 3 and 4 (especially at 11 K in Fig. 4). In order to find the frequencies of the additional mode and the subpeaks and to facilitate the peak fit, second derivatives of the Raman intensity I were calculated with respect to the Raman shift R. For the calculation of the derivatives, intensity data was slightly smoothed with the same Loess algorithm for all spectra shown in Figs. 8, 9, and 10 (and also for spectra in the intermediate-frequency region in Fig. 12). The smoothed Raman spectra together with the calculated $\partial^2 I/\partial R^2$ curves for PNZT samples with $y=0$, 0.25, and 4.0 % are shown in Figs. 8, 9, and 10, respectively, at ambient temperatures of 11, 100, 150, 200, and 295 K. Now, the peak positions in the Raman spectra are seen as minima in the second-derivative curves. The additional mode appears as a clear minimum between 50 and 60 cm^{-1} in all second-derivative curves in Figs. 8, 9, and 10. Four subpeaks were identified in the $A_1(1TO)$-mode vibrations in the $PbTiO_3$ single crystals in Ref. 11 and the results in Ref. 6 from Nd-modified $PbTiO_3$ ceramics were similar to the single-crystal results. Then, together with the $E(1LO)$ and $A_1(1LO)$ modes (at 128 and 194 cm^{-1}, respectively, at room temperature in $PbTiO_3$ single crystals[11]) there should be six peaks above the additional mode in the low-frequency region. However, there is no experimental confirmation for the $E(1LO)$- and $A_1(1LO)$-mode frequencies in PZT ceramics because of the subpeak structure of $A_1(1TO)$-mode vibrations and lack of single-crystal experiments. If the large minimum at around 140 cm^{-1} in the derivative curves in Fig. 8 is a superposition of two close minima (two solid arrows), there are six minima above the additional-mode minimum in Fig. 8. Splitting of the large minimum at around 140 cm^{-1} into two close minima is clearly seen in Fig. 9. The minimum between 90 and 100 cm^{-1} and the highest minimum at around 160 cm^{-1} (dotted arrows) in Figs. 8, 9, and 10 were so weak that it was not possible to fit these as separate peaks

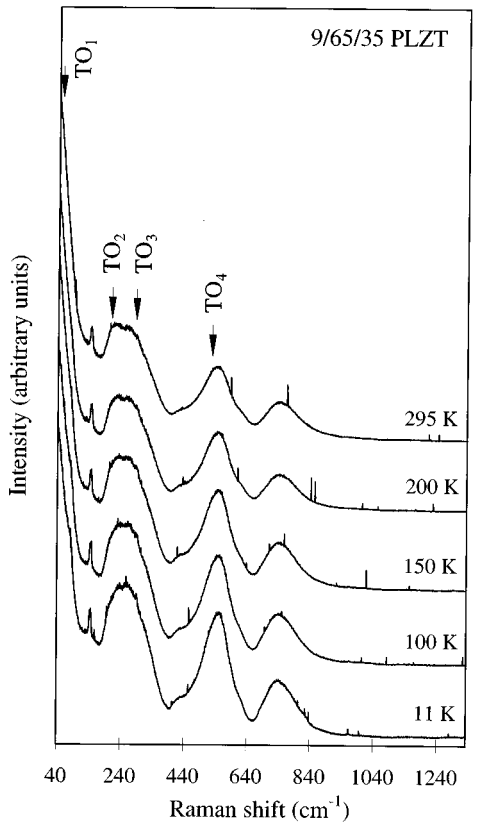

FIG. 7. Raman spectra measured at different ambient cryostat temperatures between 11 and 295 K from $Pb_{0.865}La_{0.09}(Zn_{0.65}Ti_{0.35})O_3$ (9/65/35 PLZT) relaxor ceramics. The positions of TO_1, TO_2, TO_3, and TO_4 peaks, respectively, at 50, 210, 290, and 525 cm^{-1} (Ref. 15) are also shown.

in the peak fit in Fig. 11. They may relate to the frequencies of $E(1LO)$ and $A_1(1LO)$ modes, respectively.

Gaussian line shape was used to fit the additional mode at around 55 cm^{-1} in Fig. 11. The position of this mode was very insensitive to temperature and Nd concentration y in the PNZT samples. The mode at around 115 cm^{-1} together with the weak mode between 90 and 100 cm^{-1} (Figs. 8, 9, and 10) was fitted with a single Lorentzian line shape. Attempts to use two peaks in the fit failed. Choosing a Lorentzian line shape to fit the single-crystal spectra is quite natural, since it is a limit for the damped harmonic-oscillator function, but for powder spectra it often does not give a reasonable fit. The line shape from powders is a sum of many randomly oriented grains containing also information about oblique phonons. This can lead also to asymmetric line shapes. For instance, the asymmetric line shape of the $A_1(2TO)$ mode from $PbTiO_3$ ceramics originates in oblique phonons propagating at various angles relative to the tetragonal c axis.[11] In our PNZT samples the Gaussian line shape gave usually a better fit than the Lorentzian shape. We tried also to fit the Voigt function and various approximations for it. However, all the peaks above the additional mode in Fig. 11 are fitted with Lorentzian line shapes. The background intensity was constructed in Fig. 11 from two parts using quadratic polynomials at low frequencies and linear polynomials at higher frequencies.

As discussed in Ref. 6, the low-frequency modes are of particular importance, since the soft $E(1TO)$ and $A_1(1TO)$ phonons in the tetragonal phase are in this region and, e.g., the ratio $\varepsilon(0)/\varepsilon(\infty)$ depends strongly on the frequencies of these phonons in the Lyddane-Sachs-Teller (LST) equation. Our capacitance measurements showed a substantial increase in the static dielectric constant with Nd addition both in our PNT (Ref. 6) and PNZT ceramics. An estimation of the dielectric constant, from the LST equation, of PZT ceramics with composition near the MPB, however, is very difficult. A difficulty is in the preparation of PZT single crystals for an accurate mode recognization and frequency determination. Another difficulty arises from the strong softening of the $E(1TO)$ mode in tetragonal PZT's with increasing Zr concentration and from the appearance of an additional mode between 50 and 60 cm^{-1}. There are lots of reports of the behavior of these two modes in PZT's. For instance, many reports consider the frequency behavior of the $E(1TO)$ mode when the MPB is approached from the tetragonal side in the phase diagram of PZT's. According to Refs. 17 and 18, the frequency is very small and, in fact, goes to zero at the MPB.[18] In Refs. 19 and 20, on the other hand, it was argued that the frequency does not vanish at the MPB. A strong increase in the background intensity with decreasing Raman shift in the spectra from PZT's makes an experimental verification of the frequency behavior of the $E(1TO)$ mode near the MPB very difficult. In lead titanate ceramics the corresponding background intensity is much weaker.

The $A_1(1TO)$ and $E(1TO)$ phonons at $\mathbf{k}\approx\mathbf{0}$ in the tetragonal PZT's correspond to vibrations of the lead ion with respect to the slightly distorted oxygen octahedra.[21] The displacement polarization is along a and c axes for $E(1TO)$ and $A_1(1TO)$ phonons, respectively. Our results in Ref. 6, measured form $Pb_{1-3y/2}Nd_yTiO_3$ ceramics with y between 0 and 10% at ambient temperatures between 11 K and room temperature, were in qualitative agreement with the subpeak structure reported in Ref. 11. Our fit approach in Fig. 11 for the ceramic PNZT samples also gives four subpeaks above the additional mode at Nd concentrations y below about 1.0%. The frequencies of the four fitted subpeaks in Fig. 11 are given in Table I for different Nd concentrations $y=0$, 0.25, 1.0, and 4.0 % at ambient temperatures of 11, 150, and 295 K. Only a slight increase in subpeak frequencies with decreasing temperature is seen in Table I. The frequency of the subpeak 1 is at around 145 cm^{-1} in Table I which is only about 5 cm^{-1} lower value than the corresponding frequency in the spectra from PNT samples in Ref. 6. However, the frequency difference between subpeaks 1 and 4 has increased from about 40 cm^{-1} in the PNT spectra in Ref. 6 to about 70 cm^{-1} in the PNZT spectra in Table I.

B. The intermediate-frequency region between 180 and 400 cm^{-1}

The smoothed Raman spectra together with the second-derivative curves in the intermediate-frequency region between 180 and 400 cm^{-1} are shown in Fig. 12 for PNZT samples with $y=0$, 0.25, 1.0, and 4.0 % at an ambient temperature of 11 K. The main minima in the derivative curves are also indicated with arrows. The information from the second-derivative curves in Fig. 12 was used in the peak fit

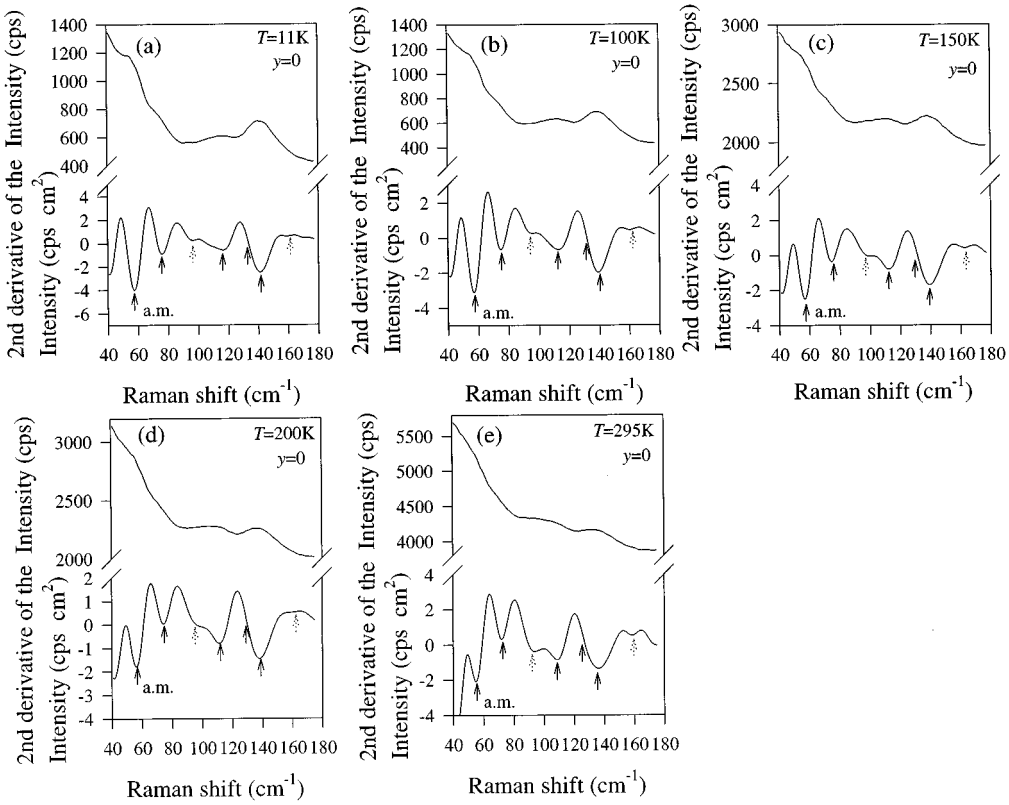

FIG. 8. Smoothed Raman spectra together with $\partial^2 I/\partial R^2$ curves in the low-frequency region from Raman measurements at ambient temperatures of (a) 11, (b) 100, (c) 150, (d) 200, and (e) 295 K from a $Pb(Zr_{0.53}Ti_{0.47})O_3$ sample ($y=0$). The subpeak structure of A_1(1TO)-mode vibrations is marked with four solid arrows and am shows the additional mode. Two dotted arrows show two extra, weak minima in the derivative curves.

of the measured Raman spectra. The results of the fit approach are shown in Fig. 13 for the Raman spectra measured at 11, 150, and 295 K from PNZT samples with Nd concentrations $y=0$, 1.0, and 4.0 %. Gaussian line shapes were used for all peaks in the fit. The two fitted peaks at around 260 and 290 cm^{-1} for the curves with $y=1.0$ and 4.0 % in Fig. 13 were constrained to have the same HWHM (half width at half maximum) value. The constrain was artificial without any physical origin, but was necessary to get a reasonable fit. Linear background intensity was used for all fits in Fig. 13. Raman spectra in the intermediate-frequency region were fitted with five different peaks, except the spectra from the pure PZT sample ($y=0$), for which it was not possible to split the strongest peak at about 280 cm^{-1} into two peaks. In the spectra of the samples with $y=1.0$ and 4.0 %, on the other hand, there are clearly two different modes at about 260 and 290 cm^{-1}. The highest mode $A_1(2)$ is also more clearly seen in Fig. 13 in the spectra of the samples with $y=1.0$ and 4.0 %.

In the intermediate-frequency region the Raman peaks originate in the splitting of the middle optical $T_{1u}(2)$ and nonpolar T_{2u} modes in the paraelectric cubic phase [the A_1(1LO) mode from the splitting of the lowest optical $T_{1u}(1)$ modes in the cubic phase is also in this region in $PbTiO_3$ (Ref. 11)]. In the tetragonal C^1_{4v} and trigonal C^1_{3v} phases the irreducible representation T_{1u} splits into $E\oplus A_1$ irreducible representations of the point groups C_{4v} and C_{3v}, respectively, whereas the irreducible representation T_{2u} splits into $E\oplus B_1$ and $E\oplus A_2$ representations of C_{4v} and C_{3v}, respectively (A_2 mode is not Raman active). Only the transverse components from the long-range Coulomb-field splitting of E and A_1 modes are in the intermediate-frequency region. We label here the Raman-active transverse E modes from T_{2u} in the tetragonal and trigonal phases by E_T and E_R (R for rhombohedral), respectively.

The second-derivative curves of the Raman spectra in Fig. 12 show two different peaks for both $E(2)$ and $A_1(2)$ symmetry modes from the splitting of $T_{1u}(2)$ modes which we label with the subscripts T and R for tetragonal and trigonal phases, respectively. The frequency of the E(2TO) mode at room temperature in tetragonal $PbTiO_3$ is 218.5 cm^{-1} (Ref. 11) and the frequency decreases with increasing Zr concentration in tetragonal PZT's.[9] Therefore, we relate the lower $E(2)$ peak at about 205 cm^{-1} to the E(2TO) peak and label it by $E(2)_T$. Then, the frequencies of the $E(2)_R$ modes in Fig. 12 are about 30 cm^{-1} higher than the $E(2)_T$ frequencies. All the frequencies inferred from Fig. 12 are given in Table II. The peak fit in Fig. 13 reveals also two separate peaks for the $E(2)$ modes, and the two different peaks are also clearly seen in the Raman spectra measured at low ambient temperatures of 11 and 150 K from the sample with $y=0$. The A_1(2TO) mode of the tetragonal $PbTiO_3$ has, at room temperature, a frequency 359.5 cm^{-1} (Ref. 11) and the frequency decreases with increasing Zr concentration in tetragonal PZT's.[9] We relate, with a caution, the higher $A_1(2)$ peaks in Fig. 12 to the tetragonal phase. The increase in the strength of the higher peak of the two $A_1(2)$ peaks with increasing Nd concentration y in Fig. 12 is then in agreement

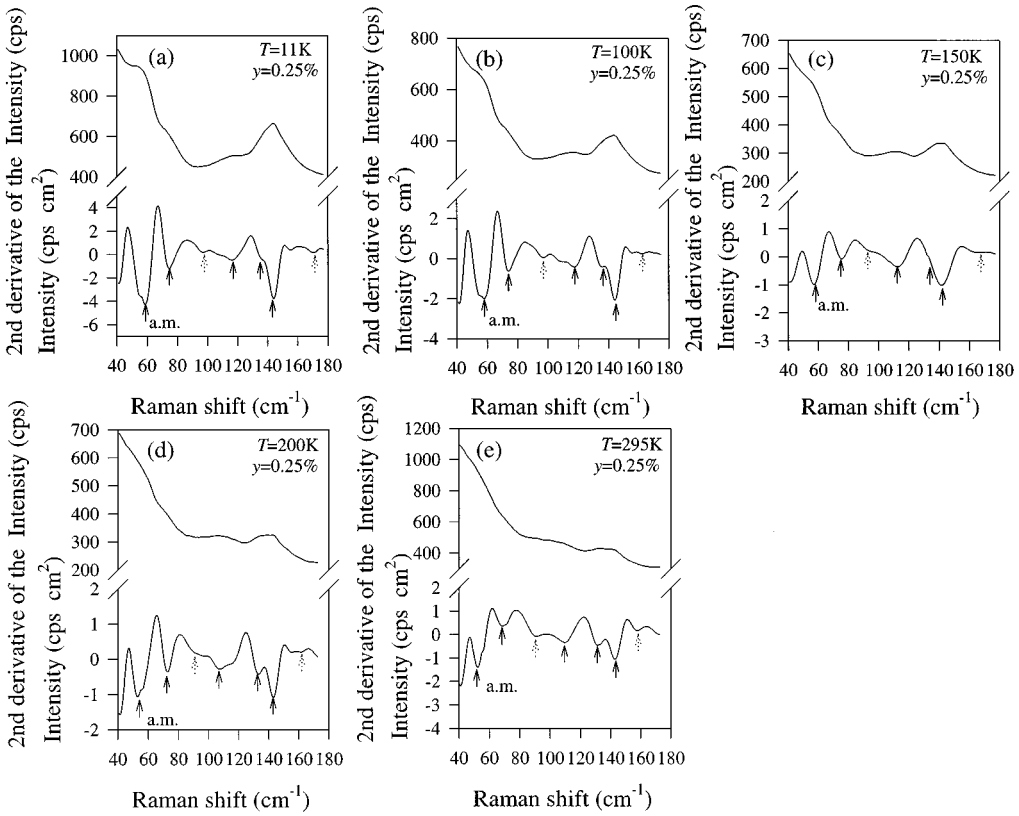

FIG. 9. Smoothed Raman spectra together with $\partial^2 I/\partial R^2$ curves in the low-frequency region from Raman measurements at ambient temperatures of (a) 11, (b) 100, (c) 150, (d) 200, and (e) 295 K from a $Pb_{0.99625}Nd_{0.0025}(Zr_{0.53}Ti_{0.47})O_3$ sample ($y=0.25\%$). The subpeak structure of $A_1(1TO)$-mode vibrations is marked with four solid arrows and am shows the additional mode. Two dotted arrows show two extra, weak minima in the derivative curves.

with the x-ray-diffraction results in Fig. 1, where the tetragonal phase fraction increases with increasing y. However, the peak fit in Fig. 13 was not successful in separating the two different $A_1(2)$ peaks.

All the four derivative curves in Fig. 12 reveal three different peaks in the region of modes from the splitting of the nonpolar T_{2u} modes. The strength of the highest peak decreases with increasing Nd concentration y and, in agreement with the x-ray-diffraction results in Fig. 1, we relate it to the trigonal E_R mode. The lower two peaks may relate to the tetragonal E_T and B_1 modes, and then the modes are not anymore degenerate in PZT ceramics at the MPB. However, it was not possible to separate these two modes in the peak fit in Fig. 13. In the case of the spectra from the sample with $y=0$ in Fig. 13, all three peaks from the splitting of the T_{2u} modes appear as a single peak in the curve fit. According to the peak assignments in Fig. 13, the intensities of the trigonal peaks decrease with the increasing Nd concentration y in agreement with the x-ray-diffraction results in Fig. 1. With decreasing temperature the intensities of trigonal peaks increase in Fig. 13 which is in agreement with the observation in Ref. 3 that the size of trigonal domains in PZT's around the MPB increases with decreasing temperature. Some of the extra peaks in the derivative curves in Fig. 12, e.g., below the $A_1(2)_R$ peak, may relate to subpeaks arising from the anharmonic contributions to the potentials.[6]

C. The high-frequency region and the high-temperature behavior

In the high-frequency region above 400 cm^{-1} the Raman spectra in Fig. 3 are characteristic to a PZT at the MPB.[22] $E(3TO)$ and $A_1(3TO)$ peaks from the tetragonal phase [at 505 and 647 cm^{-1}, respectively, in $PbTiO_3$ at room temperature (Ref. 11)] have small intensities and the strong peak at around 550 cm^{-1}, characteristic to the trigonal phase, dominates the spectra.[9] At the low ambient temperature of 11 K, in Fig. 4, the intensity of this peak is even increasing in the spectra. A strong increase in the intensity above 650 cm^{-1} with increasing Nd concentration y is also seen in the spectra in Fig. 4. This strange behaviour was not observed in the corresponding spectra from PNT ceramics.[6]

The increase in the tetragonal phase fraction with increasing temperature in Fig. 13 means that the tetragonal phase fraction may continue to increase with increasing temperature also in Figs. 5 and 6. It was found in Ref. 8 that the appearance of the tetragonal $A_1(1TO)$ peak at about 140 cm^{-1} (subpeak 1) is the most sensitive indication in the Raman spectrum at room temperature of the presence of a small tetragonal phase fraction in PZT ceramics. A decrease in the occupation of the ground level E_0 (Fig. 15) with increasing temperature may explain the decrease in the intensity of the subpeak 1 of the tetragonal $A_1(1TO)$ mode with increasing temperature in Figs. 5 and 6. In fact, the subpeak

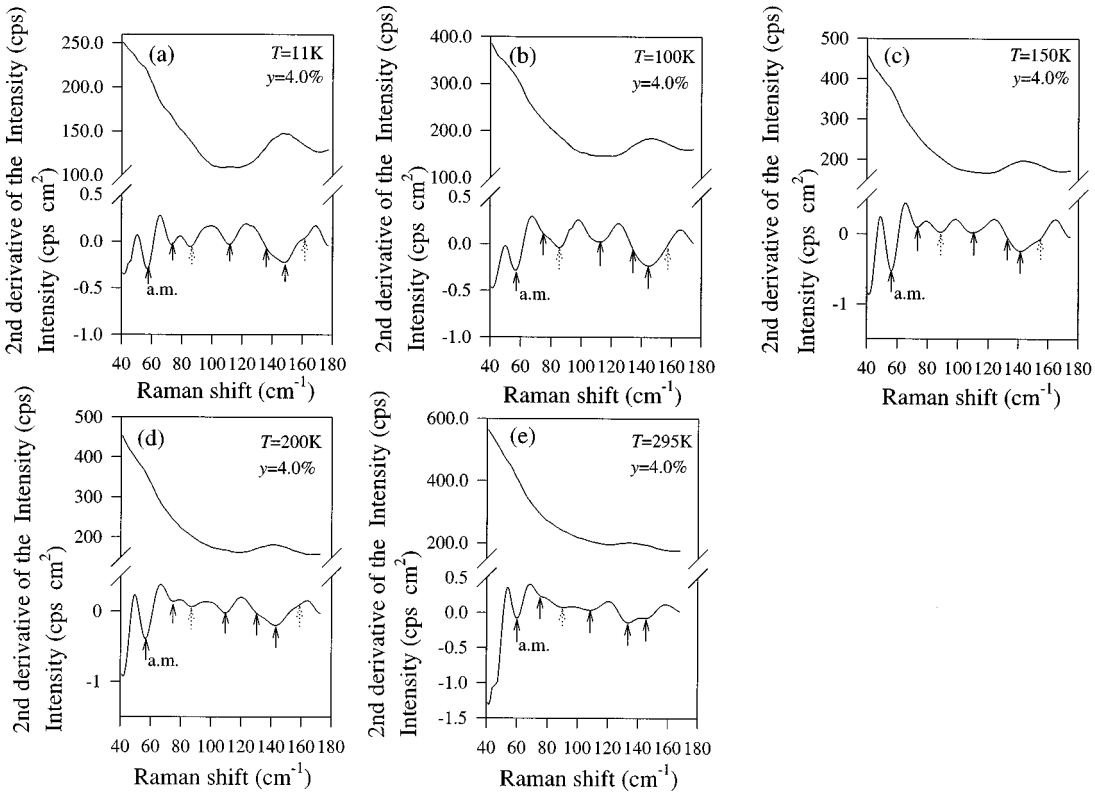

FIG. 10. Smoothed Raman spectra together with $\partial^2 I/\partial R^2$ curves in the low-frequency region from Raman measurements at ambient temperatures of (a) 11, (b) 100, (c) 150, (d) 200, and (e) 295 K from a $Pb_{0.94}Nd_{0.04}(Zr_{0.53}Ti_{0.47})O_3$ sample ($y=4.0\%$). The subpeak structure of $A_1(1\mathrm{TO})$-mode vibrations is marked with four solid arrows and am shows the additional mode. Two dotted arrows show two extra, weak minima in the derivative curves.

1 seems to disappear from the Raman spectra at 556 and 433 K in Figs. 5 and 6, respectively. A comparison of the peak structures in the intermediate-frequency range in Figs. 5 and 6 with the fitted peaks in Fig. 13, however, indicates that the trigonal phase fraction decreases with increasing temperature in Figs. 5 and 6.

The Curie temperature of PZT ceramics at the MPB is 653 K (380 °C) (Ref. 1) and Nd addition, similarly with La addition, decreases significantly the Curie temperature.[6] Therefore, the Raman spectra at 671 and 676 K, respectively, in Figs. 5 and 6 relate to the paraelectric cubic phase and then the peaks should originate in second- or higher-order processes. The intensities of the Raman peaks in the spectra above 670 K in Figs. 5 and 6, however, decreased below the values they have in the ferroelectric state (a magnification relates to these spectra in Figs. 5 and 6). Raman peaks above T_C in some $AB'_xB''_{1-x}O_3$ perovskites have been related to a possible ordered phase with the space group O_h^5 before the transformation to the disordered cubic phase with the space group O_h^1.[23,24] Raman spectra from $PbMg_{1/3}Nb_{2/3}O_3$ (PMN), $PbMg_{1/3}Ta_{2/3}O_3$ (PMT), and $PbSc_{1/2}Ta_{1/2}O_3$ (PST) ceramics were used as examples of mixed perovskites with strong Raman peaks above T_C in Refs. 23 and 24. In PST ceramics, especially, an order-disorder transformation seems possible and can be noticed also from changes in the Raman spectra.[23] However, there are no reports of a possible ordering of the B-site cations in PZT's.

PMN, PMT, and PST ceramics are also well-known relaxors similarly with the 9/65/35 PLZT ceramics in Fig. 7. There are polar nanoregions above T_C in relaxor ceramics which are the origin of the Raman peaks in the spectra above T_C. Uwe *et al.*[25] related the origin of polar nanoregions even far above the bulk T_C to symmetry-breaking defects which induce randomly oriented local domains. They determined also the size of polar nanoregions in $KTaO_3$ and found a dramatic growth in the size with decreasing temperature.[25]

Four distinct transverse optical modes above T_C are usually labeled TO_1, TO_2, TO_3, and TO_4.[26] The four modes originate in the three optical odd-parity T_{1u} and T_{2u} modes, which are not Raman active in the paraelectric cubic phase. The TO_1, TO_2, and TO_4 modes originate in the three polar T_{1u} modes, while the nonpolar T_{2u} modes are the origin of the TO_3 mode. For instance, it was found in Ref. 26 that the first-order Raman scattering from the polar TO_2 mode above and below T_C can be attributed to the presence of polar nanoregions induced by Li or Nb impurities in Li- or Nb-modified $KTaO_3$ (KLT or KTN), respectively. The TO_3 line appeared in the Raman spectra below T_C, but was missing from the spectra above T_C.[26,27] The polar TO_2 mode may couple easier than the TO_3 mode with light in the polar nanoregions.[27] However, the Raman spectra above T_C in Figs. 5 and 6 show both TO_2 and TO_3 modes. In the spectrum at 671 K in Fig. 5 from the sample with $y=0$ the stronger peak is TO_3, whereas in the spectrum at 676 K from

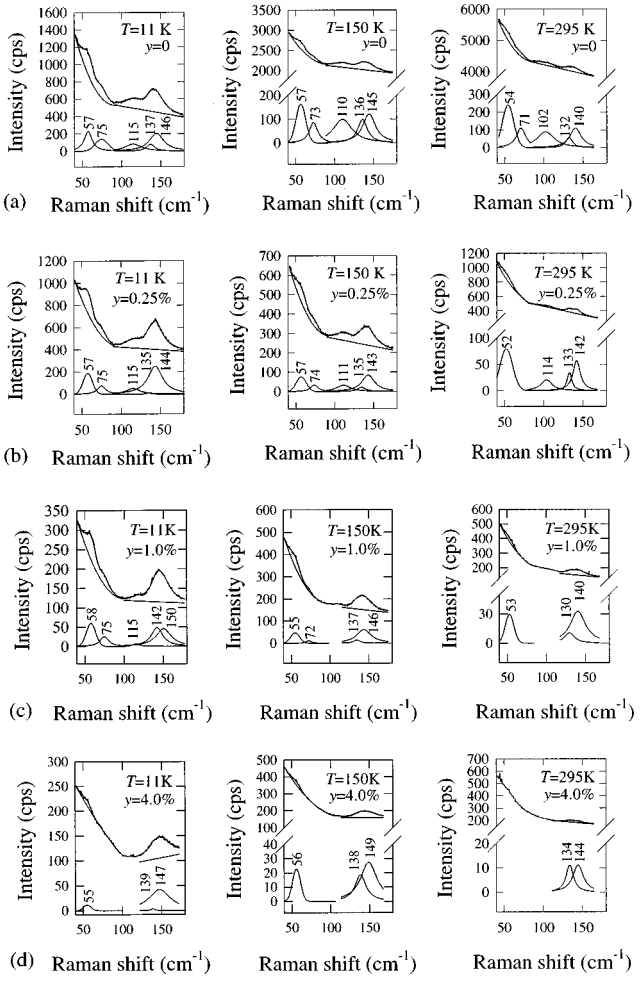

FIG. 11. Peak fit in the low-frequency region for the Raman spectra measured at ambient temperatures of 11, 150, and 295 K from $Pb_{1-3y/2}Nd_y(Zr_{0.53}Ti_{0.47})O_3$ samples with (a) $y=0$, (b) 0.25, (c) 1.0, and (d) 4.0 %. The figures show fitted peak frequencies.

TABLE I. Frequencies of the four subpeaks of A_1(1TO)-mode vibrations and the additional mode in cm^{-1} for $Pb_{1-3y/2}Nd_y(Zr_{0.53}Ti_{0.47})O_3$ samples with Nd concentrations $y=0$, 0.25, 1.0, and 4.0 % at ambient temperatures of 11, 150, and 295 K from the peak fit in Fig. 11.

		Subpeaks				Additional
T K	y %	1 cm^{-1}	2 cm^{-1}	3 cm^{-1}	4 cm^{-1}	mode $cm^{\equiv -1}$
11	0	146	137	115	75	57
	0.25	144	135	115	75	57
	1.0	150	142	115	75	58
	4.0	147	139			55
150	0	145	136	110	3	57
	0.25	143	135	111	74	57
	1.0	146	137		72	55
	4.0	149	138			56
295	0	140	132	102	71	54
	0.25	142	133	114		52
	1.0	140	130			53
	4.0	144	134			

the sample with $y=3\%$ in Fig. 6 the relative intensity of the TO_3 peak is much weaker. The frequencies of TO_2 and TO_3 peaks at about 200 and 260 cm^{-1}, respectively, in both Figs. 5 and 6 are assigned to the tetragonal phase in Fig. 13. Dai *et al.*[2] studied the normal ferroelectric to relaxor transformations in La-modified tetragonal-structured PLZT's and found it possible to induce a relaxor state at around room temperature in all tetragonal PLZT samples with increasing La content. It is possible to conclude from their tetragonal PLZT phase diagram in Ref. 2 that 3/53/47 PLZT has spontaneous relaxor to normal ferroelectric transformation at around 300 °C. Then, the temperature 563 K for a Raman spectrum in Fig. 6 is near the transformation temperature, if Nd behaves similarly with La in the PZT structure. In the transformation-temperature region domain evolution goes from polar nanodomains to tweedlike subdomain structures, and finally to normal micron-sized domains.[2]

A hint of the ordering of the normal tetragonal ferroelectric phase from the relaxor state is a splitting of the TO_4 mode into two lines.[28] The splitting is seen in the Raman spectra measured at and below 556 and 433 K in Figs. 5 and 6, respectively. A feature of the TO_4 peaks in Figs. 5 and 6 is the lack of narrowing of the lines below T_C (down to 11 K in Fig. 4). According to Marssi *et al.*,[28] the feature seems to show that the scattering process is still dominantly of the second order also below T_C and the reason for that is that the ferroelectric long-range order is not fully developed in every crystal direction. The relative intensity of the TO_4 peak is

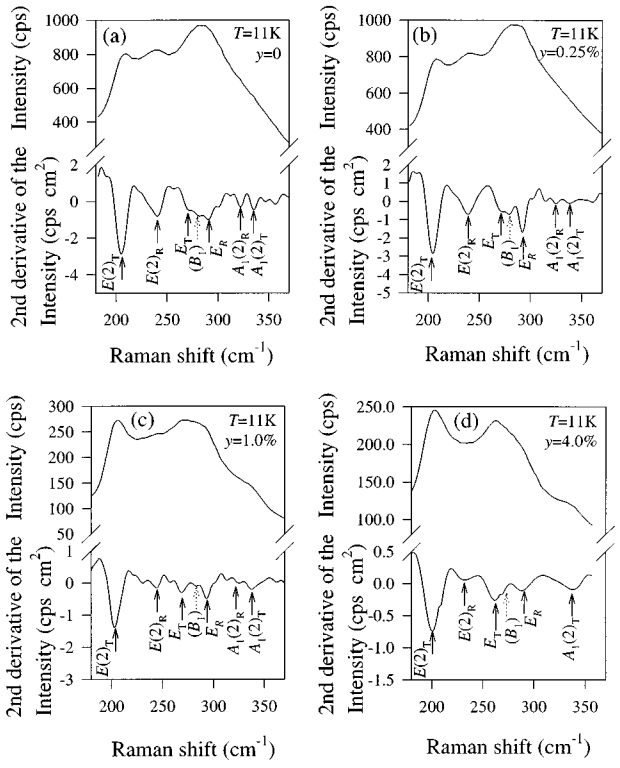

FIG. 12. Smoothed Raman spectra together with $\partial^2 I/\partial R^2$ curves in the intermediate-frequency region from Raman measurements at an ambient temperature of 11 K from $Pb_{1-3y/2}Nd_y(Zr_{0.53}Ti_{0.47})O_3$ samples with (a) $y=0$, (b) 0.25, (c) 1.0, and (d) 4.0 %. Different Raman peaks from tetragonal and trigonal phases are shown with arrows at minima in the derivative curves.

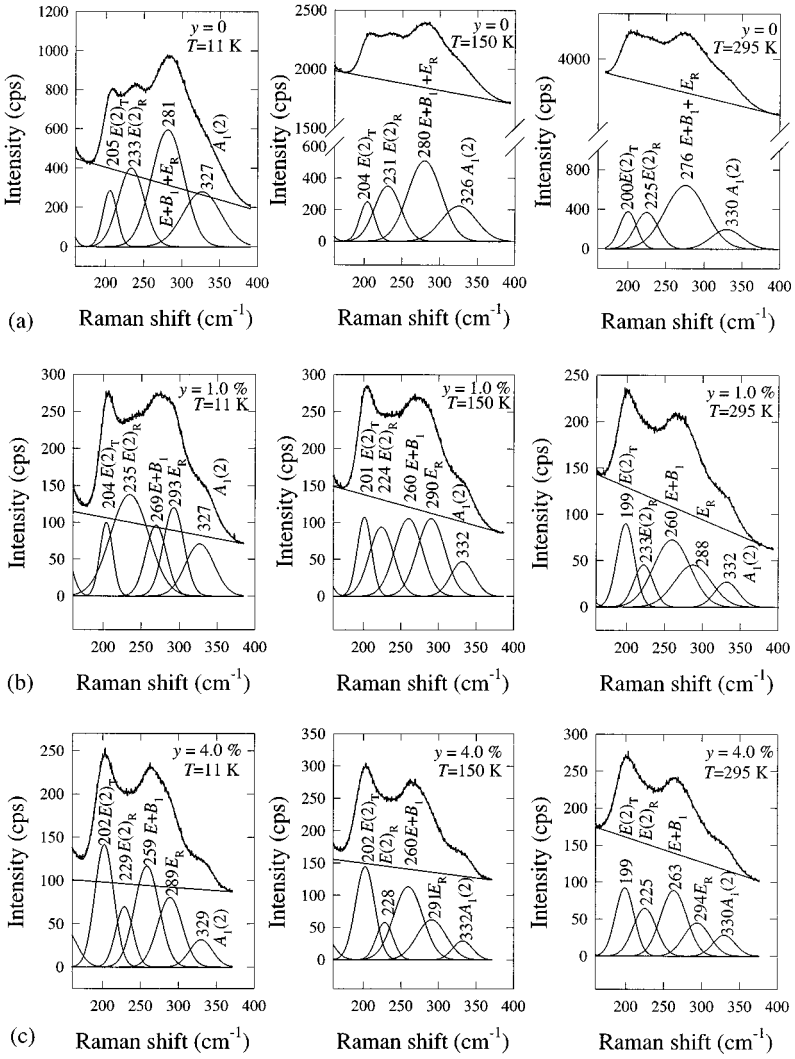

FIG. 13. Peak fit in the intermediate-frequency region for the Raman spectra measured at ambient temperatures of 11, 150, and 295 K from $Pb_{1-3y/2}Nd_y(Zr_{0.53}Ti_{0.47})O_3$ samples with (a) $y=0$, (b) 1.0, and (c) 4.0 %. The figures show fitted peak frequencies for different Raman peaks from tetragonal and trigonal phases.

seen also to increase with increasing Nd concentration y and decreasing temperature (Fig. 4).

The general shape of the high-temperature Raman spectra in Figs. 5 and 6 is very similar to the shape of the low-temperature spectra of the 9/65/35 PLZT relaxor in Fig. 7. The splitting of the TO_4 peak is not seen in the Raman spectra in Fig. 7. The relative intensity of the TO_4 peak in these spectra also increases with decreasing temperature. All the spectra in Fig. 7 have a sharp peak at about 140 cm^{-1} which is the frequency of the $A_1(1TO)$ mode in tetragonal PZT's. However, PZT ceramics with the Zr concentration of 65% have only two trigonal phases (high- and low-temperature trigonal phases with space groups C_{3v}^1 and C_{3v}^6, respectively) in the ferroelectric state. Raman spectra from both 8/65/35 and 9.5/65/35 PLZT ceramics were found to be practically identical down to an ambient temperature of 10 K in Ref. 16. At low temperatures, where the 8/65/35 ceramics has a trigonal ferroelectric phase ($T_C \approx 360$ K), Raman spectra were in favor of the high-temperature C_{3v}^1 phase and no transformation to the low-temperature C_{3v}^6 phase was found.[16] The subpeak structure of the $A_1(1TO)$ mode in Fig. 11 is also missing from the spectra in Fig. 7. A weak peak appears only at about 80 cm^{-1}. There are large differences in the low-temperature (11 K) Raman spectra at frequencies above 650 cm^{-1} between Nd- and La-modified PZT samples in Figs. 4 and 7, respectively. All the Raman spectra in Fig. 7 have only one broad peak at frequencies above 650 cm^{-1},

TABLE II. Frequencies (in cm^{-1}) of different modes inferred from the second-derivative curves in Fig. 12 for $Pb_{1-3y/2}Nd_y(Zr_{0.53}Ti_{0.47})O_3$ samples with Nd concentrations $y=0$, 0.25, 1.0, and 4.0 % at an ambient temperature of 11 K.

	Nd concentration y (%)			
Mode	0	0.25	1.0	4.0
$E(2)_T$	205	204	203	201
$E(2)_R$	240	239	244	232
E_T	273	272	269	262
(B_1)	282	279	283	271
E_R	290	292	293	288
$A_1(2)_R$	322	325	325	
$A_1(2)_T$	335	338	337	338

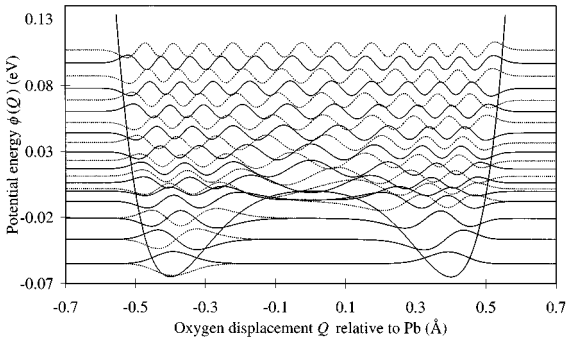

FIG. 14. Symmetric double-well potential $\phi(Q)$ fitted with Eq. (2) [$\phi(0)=0$] for A_1(1TO)-mode vibrations. The 12 lowest symmetric (solid line) and antisymmetric (dotted line) wave functions $\phi_{\nu s}$ and $\phi_{\nu a}$, respectively, are also drawn at their corresponding energy levels $E_{\nu s}$ and $E_{\nu a}$.

but the spectra from PNZT samples with Nd concentrations $y=3.0$ and 4.0 % in Fig. 4 have many different peaks in this frequency region.

V. ANHARMONICITY OF THE POTENTIAL OF A_1(1TO)-MODE VIBRATIONS

The results from the *ab initio* electronic-structure calculations in Ref. 7 for an energy decrease per primitive cell (about 0.22 eV) in the tetragonal phase of $PbTiO_3$ with $c/a=1.06$ in the case of an experimental distortion were used in Ref. 6 to construct a symmetric double-well potential energy

$$\phi(Q)=\frac{\tilde{k}_s}{2}Q^2+\frac{\xi}{4}Q^4+\frac{\zeta}{6}Q^6 \tag{2}$$

for the normal-mode coordinate Q of the A_1(1TO) mode. The anharmonic Morse potential energy from molecule vibrations was also tested in Ref. 6 and it was found that the subpeak structure is not sensitive to the shape of the anharmonic potential energy at a side minimum. However, the frequency difference between the subpeaks 1 and 4 was found to increase with decreasing well depth.

The symmetric form of the anharmonic double-well potential energy in Eq. (2) was tested also here for the A_1(1TO)-mode vibrations in the PNZT samples. An extrapolation of the atomic coordinates, obtained from neutron-diffraction studies with different PZT's of Ref. 29, gave the side minima at about $Q=\pm 40$ pm for the PZT at the MPB ($x=0.53$). The potential energy $\phi(Q)$ from Eq. (2) was fitted in Fig. 14 to give a well depth of 0.065 eV at the side minima $Q=\pm 40$ pm and a frequency 148 cm^{-1} for the A_1(1TO) subpeak 1. A reduced mass $\mu_{1TO}=75.53$ a.u. ($m_1=m_{Pb}$ and $m_2=0.53m_{Zr}+0.47m_{Ti}+3m_O$) was used in the calculations. The eigenvalues $E_{\nu s}$ and $E_{\nu a}$ for symmetric and antisymmetric eigenfunctions $\phi_{\nu s}$ and $\phi_{\nu a}$, respectively, calculated from the double-well potential energy in Fig. 14 up to $\nu=11$ by a numerical solution of the Schrödinger equation for the A_1(1TO)-mode vibrations are given in Table III together with the different subpeak frequencies (Stokes transitions between levels). The differences in the eigenvalues E_ν between symmetric and antisymmetric eigen-

TABLE III. Eigenvalues $E_{\nu s}$ and $E_{\nu a}$ up to $\nu=11$ for symmetric and antisymmetric eigenfunctions $\phi_{\nu s}$ and $\phi_{\nu a}$, respectively, calculated with the symmetric double-well potential in Fig. 14 for the A_1(1TO)-mode vibrations, together with frequencies for different $\nu_j-\nu_i$ subpeaks (Stokes transitions from level ν_j to ν_i). The calculated values of relative matrix elements $|\langle\phi_{\nu_j}|Q|\phi_{\nu_i}\rangle|/|\langle\phi_1|Q|\phi_0\rangle|$ are also given for different $\nu_j-\nu_i$ subpeaks together with the relative Raman (Stokes) intensities at 295 K from both numerical calculations and Eq. (4).

ν	$E_{\nu s}$ meV	$E_{\nu a}$ meV	Subpeak $\nu_j-\nu_i$	Frequency cm^{-1}	Matrix element relative	Relative intensity calculated	Eq. (4)
0	−55.05	−55.05	1−0 (1)	148	1.00	1.00	1.00
1	−36.66	−36.66	2−1 (2)	129	1.46	1.04	0.97
2	−20.72	−20.72	3−2 (3)	104	1.85	0.89	0.71
3	−7.89	−7.84	$4a-3s$ (4)	78	2.19	0.38	0.46
			$4s-3a$ (4)	62	2.21	0.38	
4	0.18	1.75	$4a-4s$	16	4.45	1.06	
			$5s-4a$	37	4.33	1.01	0.28
5	6.28	11.23	$5a-5s$	40	4.69	0.99	
			$6s-5a$	45	4.98	0.92	0.16
6	16.84	22.99	$6a-6s$	50	5.17	0.79	
			$7s-6a$	54	5.33	0.66	0.09
7	29.63	36.72	$7a-7s$	57	5.46	0.54	
			$8s-7a$	60	5.57	0.42	0.05
8	44.24	52.11	$8a-8s$	64	5.67	0.33	
			$9s-8a$	67	5.57	0.25	0.03
9	60.39	69.02	$9a-9s$	70	5.85	0.19	
			$10s-9a$	72	5.93	0.14	0.02
10	77.99	87.31	$10a-10s$	75	6.00	0.10	
			$11s-10a$	78	6.07	0.07	0.01
11	96.94	106.89	$11a-11s$	80	6.13	0.05	

functions are less than 1 cm^{-1} up to $\nu=3$. Symmetric and antisymmetric eigenfunctions $\phi_{\nu s}$ and $\phi_{\nu a}$, respectively, up to $\nu=11$ are also shown in Fig. 14, drawn at their corresponding energy levels E_ν (with horizontal (zero) part of the eigenfunctions outside the double-well potential).

The calculated four uppermost subpeak frequencies in Table III fit qualitatively the observed frequencies in Table I. The frequency of the subpeak 1 in Table III is 148 cm^{-1} which is in the region of the observed frequencies of subpeak 1 between 144 and 150 cm^{-1} at 11 K in Table I, and the frequency of the subpeak 4 in Table III is 78 cm^{-1} ($E_{4a}-E_{3s}$) which is also close to the observed frequency of 75 cm^{-1} of the subpeak 4 at 11 K in Table I.

Another alternative for the frequency of the subpeak 4 in Table III is 62 cm^{-1} which corresponds to the Stokes transition between E_{4s} and E_{3a} levels. This is a feature from the approach with the symmetric double-well potential which, in fact, is valid only at (or above) the Curie temperature T_C. It can be used, as a first approximation also below T_C, when considering the local phonon excitations inside a side minimum. The deeper side minima in Nd-modified $PbTiO_3$ made it possible in Ref. 6 to use a symmetric double-well potential energy to get unique values for all four subpeak frequencies.

Below T_C the electric polarization breaks the symmetry of the double wells, causing the order parameter of the structural phase transition within the framework of Landau's theory.[12] For modeling a ferroelectric transition with an oscillator moving in a one-dimensional potential, the expectation value $\langle Q\rangle$ of the normal-mode coordinate is an order parameter which is proportional to the mean displacement of the ions from the centrosymmetric positions and proportional to the mean polarization of the unit cell. In the mean-field approach[30,31] a linear coupling term is added to the symmetric double-well potential energy [Eq. (2)] to describe the interactions with the surrounding unit cells. Then the Schrödinger equation has to be solved with a potential energy

$$\phi(Q)=\frac{\tilde{k}_s}{2}Q^2+\frac{\xi}{4}Q^4+\frac{\zeta}{6}Q^6+\chi\langle Q\rangle Q, \tag{3}$$

where χ is a coupling constant which would produce the proper order parameter. Above T_C, the order parameter $\langle Q\rangle$ is zero and the potential energy is symmetric about $Q=0$, but below T_C the intercell coupling term breaks the symmetry of the potential.

The potential energy in Eq. (3) depends indirectly on temperature through the value $\langle Q\rangle$ and the phase transition will be an intermediate between displacive and order-disorder in the case where the barrier between the wells is not very high. Using a Boltzmann distribution for the occupation of levels, a self-consistent calculation of $\langle Q\rangle$ at different temperatures makes it possible to study the temperature dependence of the dielectric response and the spontaneous polarization of linear ferroelectrics.[12,32] We tested also the potential in Eq. (3) in order to fit the subpeaks of the A_1(1TO)-mode vibrations in Table I. In fact, in tetragonal PZT's the polarization originates in the displacement of Pb^{2+} ions with respect to the slightly distorted oxygen octahedra [A_1(1TO) mode] and in the displacement of Ti^{4+} (and Zr^{4+}) ions inside the distorted oxygen octahedra [A_1(2TO) mode]. In $PbTiO_3$, for instance, the Pb^{2+}-ion displacement (47 pm) is roughly 1.5 times larger than that of Ti^{4+} ion (30 pm) and the Pb^{2+} ions contribute 46% of the saturation polarization.[14]

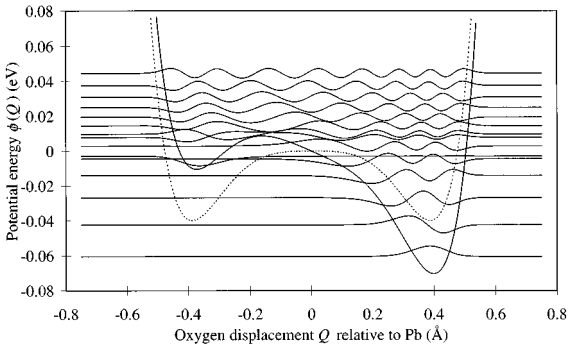

FIG. 15. Asymmetric double-well potential $\phi(Q)$ (solid line) fitted with Eq. (3) [$\phi(0)=0$] for A_1(1TO)-mode vibrations together with the symmetric part of the potential energy (dotted line). The 15 lowest wave functions ϕ_ν are also drawn at their corresponding energy levels E_ν.

Therefore, the temperature dependence of the potential in Eq. (3) is only an approximation for PZT's. However, the displacement of Pb^{2+} ions is more sensitive to temperature[14] and stabilizes the tetragonal phase.[7] The asymmetric potential in Eq. (3), used for testing the A_1(1TO)-mode vibrations in our PNZT samples with coefficients $\tilde{k}_s/2=-0.03439$ eV/Å^2, $\xi/4=-4.86803$ eV/Å^4, $\zeta/6=22.1555$ eV/Å^6, and $\chi\langle Q\rangle=-0.0775$ eV/Å, is shown in Fig. 15 together with its symmetric double-well part. The value 0.04 eV for the barrier height between the two wells in the symmetric part of the potential in Fig. 15 is, to some extent, larger than the value $k_BT_C/2=327$ K$=0.028$ eV, as assumed in Ref. 33. The coefficients of the potential in Fig. 15 were fitted to give a minimum of the deeper lobe at $Q\approx0.4$ Å and approximately the fitted frequencies in Fig. 11 for the subpeaks 1 and 4. The 15 lowest eigenfunctions ϕ_ν from a numerical solution of the Schrödinger equation are also shown in Fig. 15, drawn at their corresponding energy levels E_ν [with horizontal (zero) parts of eigenfunctions outside the potential wells]. The calculated eigenvalues E_ν up to $\nu=13$ together with the different subpeak frequencies (Stokes transitions between levels) are given in Table IV. The frequencies of the subpeaks 1–4 are in close agreement with the corresponding subpeak frequencies in Table III, calculated from the symmetric double-well potential in Fig. 14, which shows again that the subpeak frequencies are insensitive to the shape of the potential in a lobe.

In the anharmonic potential model for subpeaks, the intensity of a given Stokes transition from level ν_j to ν_i is proportional to the population of the initial level ν_i and to the square of the matrix element $\langle\phi_{\nu_j}|Q|\phi_{\nu_i}\rangle$ (dipole transition). In the case of a harmonic oscillator, transitions are allowed only between adjacent energy levels and the matrix element is proportional to $\sqrt{n+1}$ for the transition from $n+1$ to n. The relative intensity R of the Stokes transition from level $n+1$ to n to that of the 1 to 0 transition is now given by the equation[11]

$$R=(n+1)\exp[-n\hbar\omega/(k_BT)], \tag{4}$$

where, for the A_1(1TO) mode in Fig. 15, $\hbar\omega$ is 146 $cm^{-1}=209$ K. At room temperature, the fitted relative intensities of the subpeaks 1–4 of samples with $y=0$ and

TABLE IV. Eigenvalues E_ν up to $\nu=13$, calculated from the asymmetric double-well potential in Fig. 15 for the A_1(1TO)-mode vibrations, together with frequencies for different $\nu_j-\nu_i$ subpeaks (Stokes transitions from level ν_j to ν_i). The calculated values of relative matrix elements $|\langle\phi_{\nu_j}|Q|\phi_{\nu_i}\rangle|/|\langle\phi_1|Q|\phi_0\rangle|$ are also given for different $\nu_j-\nu_i$ subpeaks together with the relative Raman (Stokes) intensities at 295 K from both numerical calculations and Eq. (4).

ν	E_ν meV	Subpeak $\nu_j-\nu_i$	Frequency cm^{-1}	Matrix element relative	Relative intensity calculated Eq. (4)	
0	−60.55	1−0 (1)	146	1.00	1.00	1.00
1	−42.45	2−1 (2)	126	1.46	1.05	0.98
2	−26.82	3−2 (3)	103	1.86	0.92	0.72
3	−14.09	4−3 (4)	78	2.24	0.81	0.47
4	−4.47	5−4	12	0.07	0.00	0.29
		6−4	59	2.67	0.79	
5	−2.98	6−5	47	0.13	0.00	0.17
		7−5	88	0.87	0.08	
6	2.81	7−6	41	2.33	0.45	0.10
7	7.89	8−7	15	4.58	1.42	0.06
8	9.78	9−8	39	4.30	1.16	0.03
9	14.59	10−9	39	4.74	1.17	0.02
10	19.47	11−10	44	4.99	1.07	0.01
11	24.98	12−11	49	5.16	0.92	
12	31.05	13−12	53	5.30	0.75	
13	37.60	14−13	56	5.42	0.62	

0.25 % in Fig. 11 are in qualitative agreement with the values obtained from Eq. (4) in Tables III and IV. For instance, the intensity of the subpeak 4 at room temperature of the sample with $y=0$ should be about one half of the intensity of the subpeak 1 according to Eq. (4). Because of the decreasing ''ladder steps'' between the energy levels E_ν, however, the energy level E_3 is $(140+132+102)=374\ cm^{-1}$, instead of $3\times140=420\ cm^{-1}$ in Eq. (4), above the ground level E_0 for the sample with $y=0$ at 295 K in Table I. The matrix element for the transitions from $n+1$ to n increases also faster than $\sqrt{n+1}$ in Eq. (4) with increasing n, e.g., in the deeper lobe of the anharmonic potential in Fig. 15 (see Table IV). With these two corrections to Eq. (4), the above intensity ratio between subpeaks 4 and 1 should be about 0.8 instead of 0.5 from Eq. (4). The increase in the discrepancy with decreasing temperature between the subpeak intensities fitted in Fig. 11 and calculated from Eq. (4) may originate in the excitation of phonons (local heating) by the laser light, as discussed in Ref. 6. The intensity ratios between subpeaks 2 and 1 for the sample with $y=4.0\%$ in Fig. 11 are in close agreement with the values 1.0 and 0.5 from Eq. (4), respectively, at 295 and 150 K. The subpeak frequencies in Fig. 11 are insensitive to the Nd addition. However, the subpeak intensities decrease with the Nd addition and their mutual intensities also change. Relative matrix elements $|\langle\phi_{\nu j}|Q|\phi_{\nu i}\rangle|/|\langle\phi_1|Q|\phi_0\rangle|$, calculated with the eigenfunctions ϕ_ν from the numerical solutions for the potential energies in Figs. 14 and 15, are given for different $\nu_j-\nu_i$ subpeak transitions in Tables III and IV, respectively. The relative Raman intensities of the subpeaks from the multiplication of the squares of the matrix elements by the corresponding Boltzmann factors for the thermal population of levels in the Stokes transitions at 295 K are also given in Tables III and IV together with the corresponding relative intensities calculated from Eq. (4). Large matrix elements appear in Tables III and IV for the transitions between delocalized vibrational levels and, therefore, there are many $\nu_j-\nu_i$ transitions with low frequencies below the frequency of the subpeak 4, which also have, at 295 K, higher intensities than the intensity of the subpeak 1 (Table IV).

The low-frequency Raman spectra from PZT ceramics differ, to a large extent, from the spectra measured from lead-titanate ceramics. In the spectra from Nd-modified $PbTiO_3$ ceramics in Ref. 6, there is only the E(1TO) peak at around $80\ cm^{-1}$ together with a slight and flat background intensity below the four A_1(1TO) subpeaks. In the spectra in Fig. 11, however, the low-frequency background increases strongly with decreasing Raman shift. For instance, static imperfections have been related to the origin of this strong ''central mode.'' [34] An oscillator moving in a damped asymmetric double-well potential [Eq. (3)] was used in Ref. 12 to reproduce the high-intensity ''central peak'' appearing in many ferroelectrics. Below T_C the linear term in the potential in Eq. (3) breaks the symmetry of the double wells, causing the order parameter and the spacing between the symmetric and antisymmetric energy levels of the paraelectric phase to increase in the deeper lobe of a double-well potential with a relatively shallow well depth. Similarly, we get a central peak at $0.4\ cm^{-1}$ from the $3a$-$3s$ transition (Table III) in the potential in Fig. 14 with a deep well depth of 0.065 eV. A ''central peak'' at $16\ cm^{-1}$ in Table III originates in the large matrix element between the close energy levels E_{4a} and E_{4s} around the top of the barrier between the two wells in the potential in Fig. 14. In fact, we found some peaks to appear at about $20\ cm^{-1}$ in some Raman spectra from our PNZT samples, as shown in the two spectra in Fig. 16. The energy levels E_5 and E_4 in the potential in Fig. 15 have an energy splitting of only $12\ cm^{-1}$. The transition between these lev-

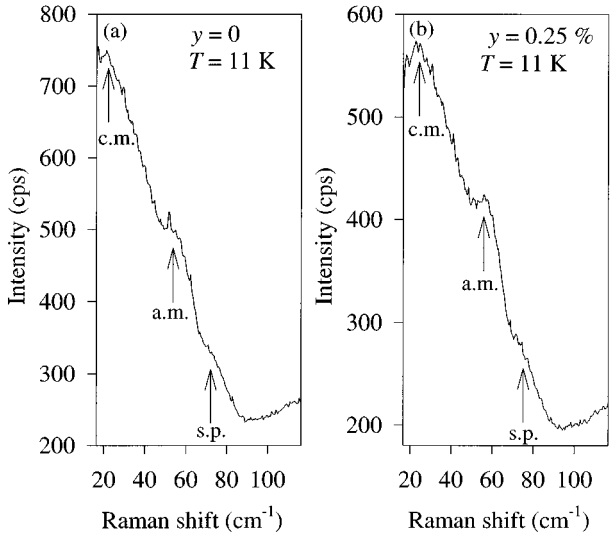

FIG. 16. Low-frequency Raman spectra above 20 cm^{-1}, measured at an ambient temperature of 11 K from $Pb_{1-3y/2}Nd_y(Zr_{0.53}Ti_{0.47})O_3$ samples with (a) $y=0$ and (b) 0.25 %. Arrows show the positions of a ''central mode'' (cm), the additional mode (am), and subpeak 4 (sp) in both spectra.

els can be interpreted as a tunneling resonance between the two lobes in the potential. For instance, the observed weak resonance at 1 THz (32 cm^{-1}) in $LiTaO_3$ was related to a corresponding tunneling resonance between two lobes in the potential in Ref. 32. The matrix element of the 5-4 transition in Table IV, however, is very small which means that this tunneling resonance is very weak. The energy levels E_8 and E_7 at the top of the barrier between the two potential lobes in Fig. 15 have also a small energy split of 15 cm^{-1}. The 8-7 Stokes transition has now a large matrix element and its intensity at room temperature in Table IV is 42% higher than the intensity of the subpeak 1.

In the Raman spectra in Fig. 11 from our PNZT samples an ''additional mode'' appears between 52 and 58 cm^{-1} (Table I). The mode seems to be closely related to the structure of the four $A_1(1TO)$ subpeaks in Fig. 11 and, therefore, its frequency is insensitive to both temperature and the Nd concentration y. The intensity of the mode decreases with decreasing temperature and increasing Nd concentration y. An additional mode with E symmetry was found in the Raman spectra from $Pb(Ti_{0.81}Sn_{0.19})O_3$ single crystals.[20] The Raman spectra in Fig. 7 from 9/65/35 PLZT ceramics show only a low-frequency peak at around 80 cm^{-1} below a very sharp peak at about 140 cm^{-1}. However, an additional mode was reported to appear between 50 and 60 cm^{-1} in the Raman spectra from $Pb_{0.85}La_{0.10}TiO_3$ ceramics in Refs. 20 and 35. There are many suggestions for the origin of the additional mode in the literature. A coupling of the zone-boundary transverse acoustical phonons with $E(1TO)$ phonons at $\mathbf{k}\approx\mathbf{0}$ was suggested in Ref. 35, and the origin is also related alone to zone-boundary transverse acoustical phonons which become Raman active by the absence of translational symmetry[18] or due to Zr ''impurities.'' [19] Bäuerle *et al.*[19] consider also the possibility that the mode might arise from the localized vibrations associated with oxygen vacancies which are known to exist often in mixed systems. The Nd_2O_3 and La_2O_3 additions into PZT are known to remove the oxygen vacancies from the structure and should therefore decrease the intensity of the additional mode.

Our results in Tables III and IV give an explanation for the appearance of the additional mode. In the case of the symmetric double-well potential in Fig. 14 there are many Stokes transitions between delocalized levels in Table III which have high intensities at frequencies between 40 and 70 cm^{-1}. A broad ''additional-mode'' peak at around 55 cm^{-1} should now appear in the Raman spectrum from the oscillator-vibrations at room temperature. In the case of the asymmetric potential in Fig. 15 there are many Stokes transitions between delocalized levels in Table IV with high intensities at frequencies between 39 and 59 cm^{-1} which together form an ''additional-mode'' peak at around 50 cm^{-1}. We believe that with proper values for the coefficients in the potential in Eq. (3) it is possible to fit the additional mode (and also some central peaks) at the observed frequencies in Table I. For instance, the value 0.04 eV taken for the well depth in the symmetric part of the potential in Fig. 15 is rather arbitrary.

The Stokes transition 5-4 in Table IV, corresponding to the tunneling resonance between the deeper lobe and the more shallow lobe in Fig. 15, has a very weak intensity, but the intensity of the 6-4 transition is larger by a factor of 1455. However, the matrix element for transitions (Stokes or anti-Stokes) between levels E_6 and E_5 is also small in Table IV. Therefore, the occupation of the nearly localized level E_5 in the shallow lobe originates in the anti-Stokes transitions from delocalized levels above E_6 and, correspondingly, the excitation of vibrations at level E_5 takes place to delocalized levels above E_6. For instance, the Stokes transition 7-5 having a frequency of 88 cm^{-1} (in the region of a weak derivative peak in Figs. 8, 9, and 10) has a relative intensity 0.08 in Table IV. It follows that the shallow lobe in Fig. 15 has an effect to increase the Raman intensity of the transitions between delocalized levels during the laser-light irradiation.

VI. CONCLUSIONS

Detailed Raman studies have been reported on the optical phonons of lead zirconate titanate ceramics at the morphotropic phase boundary with different Nd-additive concentrations between 0 and 4% of the A-cation sites. Raman spectra were measured at various temperatures from above the Curie temperature T_C down to a low cryostat temperature of 11 K. However, a considerable phonon excitation by laser light, corresponding to local heating, was apparent at low cryostat temperatures from the measured intensity ratios between the anti-Stokes and Stokes lines in Eq. (1) (compare Ref. 6). Raman modes from both tetragonal and trigonal phases were present in the spectra. Some extra unknown Raman peaks were also found to increase at high frequencies above 650 cm^{-1} with increasing Nd concentration and decreasing temperature (Fig. 4). It was found from the x-ray-diffraction experiments that the tetragonal phase fraction increased with increasing Nd addition. The tetragonal c/a ratio also increased with increasing Nd concentration below 1% (Fig. 2). However, the Nd addition did decrease the intensities of the

tetragonal $A_1(1\mathrm{TO})$-mode subpeaks, which were revealed by the second derivatives of the Raman spectra and a peak-fit approach (Fig. 11) from all Raman spectra measured at and below room temperature. It was also possible to construct an anharmonic double-well potential for the $A_1(1\mathrm{TO})$-mode vibrations both in symmetric and asymmetric [from the mean-field approach (Ref. 12)] forms to fit approximately the revealed subpeak structure. The second derivatives of the Raman spectra together with a peak fit were also used to identify the peak structure of the Raman spectra in the intermediate-frequency region between 180 and 400 cm^{-1}. Raman spectra measured from 9/65/35 PLZT relaxor ceramics were used as a reference for the discussion of the high-temperature Raman spectra measured up to a temperature above T_C.

ACKNOWLEDGMENTS

We wish to thank Dr. K. Lubitz for his kind supply of the PNZT samples for this study. T. Murtoniemi and E. Siren are acknowledged for their help in constructing the cooling system used in the Raman measurements, J. Levoska for discussions concerning x-ray-diffraction measurements, and Dr. L. Pirttiaho for discussing the paper. J.F. acknowledges the financial support of the foundation Tekniikan Edistämissäätiö in Finland.

[1] B. Jaffe, W. R. Cook, and H. Jaffe, *Piezoelectric Ceramics* (Academic, London, 1971).
[2] Xunhu Dai, Z. Xu, and Dwight Viehland, J. Appl. Phys. **79**, 1021 (1996).
[3] Qi Tan and Dwight Viehland, Phys. Rev. B **53**, 14 103 (1996).
[4] Dwight Viehland and Jie-Fang Li, J. Appl. Phys. **75**, 1705 (1994).
[5] I. M. Reaney, J. Petzelt, V. V. Voitsekhovskii, F. Chu, and N. Setter, J. Appl. Phys. **76**, 2086 (1994).
[6] J. Frantti and V. Lantto, Phys. Rev. B **54**, 12 139 (1996).
[7] R. E. Cohen, Nature (London) **358**, 136 (1992).
[8] J. Frantti, V. Lantto, and J. Lappalainen, J. Appl. Phys. **79**, 1065 (1996).
[9] J. Frantti, V. Lantto, and J. Lappalainen, Ferroelectrics **184**, 69 (1996).
[10] Gerald Burns and Bruce A. Scott, Phys. Rev. B **7**, 3088 (1973).
[11] C. M. Foster, Z. Li, M. Grimsditch, S. K. Chan, and D. J. Lam, Phys. Rev. B **48**, 10 160 (1993).
[12] J. W. Flocken, R. A. Guenther, J. R. Hardy, and L. L. Boyer, Phys. Rev. B **40**, 11 496 (1989).
[13] M. Dvoršek, M.Sc. thesis, University of Ljubljana, Ljubljana, 1989; M. Kosec, M. Dvoršek, M. Pristavec, V. Kraševec, and D. Kolar (unpublished).
[14] W. L. Warren, J. Robertson, D. Dimos, B. A. Tuttle, and G. E. Pike, Phys. Rev. B **53**, 3080 (1996).
[15] A. Lurio and G. Burns, J. Appl. Phys. **45**, 1986 (1974).
[16] J. Pokorný, J. Petzelt, I. Gregora, V. Železný, V. Vorlíček, Z. Zikmund, I. Fedorov, A. Pronin, and M. Kosec, Ferroelectrics **186**, 115 (1996).
[17] A. Pinczuk, Solid State Commun. **12**, 1035 (1973).
[18] R. Merlin and A. Pinczuk, Ferroelectrics **7**, 275 (1975).
[19] D. Bäuerle, Y. Yacoby, and W. Richter, Solid State Commun. **14**, 1137 (1974).
[20] G. Burns and F. H. Dacol, Solid State Commun. **18**, 1325 (1976).
[21] J. D. Freire and R. S. Katiyar, Phys. Rev. B **37**, 2074 (1988).
[22] Shu Li, R. A. Condrate, Sr., and R. M. Spriggs, Can. Ceram. Q. **55**, 61 (1988).
[23] I. G. Siny and T. A. Smirnova, Ferroelectrics **90**, 191 (1989).
[24] I. G. Siny and C. Boulesteix, Ferroelectrics **96**, 119 (1989).
[25] H. Uwe, K. B. Lyons, H. L. Carter, and P. A. Fleury, Phys. Rev. B **33**, 6436 (1986).
[26] P. DiAntonio, B. E. Vugmeister, and J. Toulouse, Phys. Rev. B **47**, 5629 (1993).
[27] J. Toulouse, P. DiAntonio, B. E. Vugmeister, X. M. Wang, and L. A. Knauss, Phys. Rev. Lett. **68**, 232 (1992).
[28] M. El Marssi, R. Farhi, X. Dai, A. Morell, and D. Viehland, J. Appl. Phys. **80**, 1079 (1996).
[29] B. Morosin, A. C. Lawson, G. H. Kwei, J. A. Voigt, and B. A. Tuttle, in *Neutron Scattering in Materials Science II*, edited by D. A. Neumann, J. P. Russell, and B. J. Wuensch, MRS Symposia Proceedings No. 376 (Materials Research Society, Pittsburgh, 1995), p. 609.
[30] T. R. Koehler and N. S. Gillis, Phys. Rev. B **9**, 4980 (1972).
[31] N. S. Gillis and T. R. Koehler, Phys. Rev. B **7**, 3806 (1974).
[32] H. J. Bakker, S. Hunsche, and H. Kurz, Phys. Rev. B **48**, 9331 (1993).
[33] S. C. Abrahams, S. K. Kurtz, and P. B. Jamieson, Phys. Rev. **172**, B551 (1968).
[34] Gerald Burns, *Solid State Physics* (Academic, London, 1985).
[35] R. Merlin, J. A. Sanjurjo, and A. Pinczuk, Solid State Commun. **16**, 931 (1975).